EFFECT OF THE POROSITY ON THE FATIGUE STRENGTH OF METALS

Sabrina Vantadori[a], Camilla Ronchei[b,*], Daniela Scorza[c],

Andrea Zanichelli[a], Raimondo Luciano[c]

[a] Department of Engineering & Architecture, University of Parma,
Parco Area delle Scienze 181/A, 43124 Parma, Italy

[b] Department of Civil Engineering, University of Calabria,
via Pietro Bucci, 87036 Arcavacata di Rende (CS), Italy

[c] Department of Engineering, University of Naples Parthenope,
Centro Direzionale Isola C4, 80143 Napoli, Italy

*Corresponding author: *camilla.ronchei@unical.it*

ABSTRACT

In the present paper a procedure for fatigue strength assessment of metals containing solidification defects is employed to analyse the fatigue behaviour of a ductile cast iron (DCI) characterised by a relevant micro-shrinkage porosity. The procedure implements: (i) a statistical method deriving from extreme value theory, (ii) the $\sqrt{area}$ -parameter model, and (iii) the multiaxial critical plane-based criterion by Carpinteri at al. According to the above statistical method, both the distribution of defects and the return period are determined. More precisely, the return period is computed by also exploiting a relationship here proposed to optimise the accuracy of the procedure in terms of fatigue strength estimation. The great potential of the present procedure is that the defect content analysis (performed by means of a statistical method deriving from extreme value theory) can be easily performed using machine learning techniques.

KEYWORDS: Ductile Cast Iron; extreme value theory; infinite fatigue life; solidification defects; statistical method

1. INTRODUCTION

Ductile Cast Iron (DCI) is a cast iron with a microstructure characterised by small spherical graphite particles embedded in a matrix, which is usually ferritic and/or pearlitic, depending on alloy composition, casting control and final heat treatment[1]. Other names of DCI are nodular, spherulitic and spheroidal cast iron.

Over the last years, the fabrication of heavy section DCI components (i.e. DCI components of weight on the order of tens of tons) for structural purposes has increased due to the favourable combination of both mechanical and technological properties and low production costs. As a matter of fact, DCI is widely used in the critical automotive parts (as crankshafts), big engine blocks, parts of hydraulic presses, canisters for nuclear waste storage and wind turbines[2]. In order to give an order of magnitude of the material quantity involved in the production of heavy section components, a single wind turbine contains approximately 10-25 tons of DCI.

As pointed out by Benedetti et al.[3] and Borsato et al.[4], heavy section casting involves long solidification times with the consequence that a fully control of casting quality is not possible, that is, the microstructure of the DCIs cannot be controlled. It is well known that the microstructure depends on several factors, and more precisely: alloying elements, casting temperature, cooling rate and spheroidization of graphite[5].

The DCI microstructure can be efficiently controlled in small DCI components, whereas in real components (such as heavy section DCI components) the control of the microstructure during solidification and cooling is rather difficult, thus introducing in the material solidification defects in terms of shrinkage porosity. For example, **Figure 1** shows the fracture surface SEM images (at different magnification levels) of some DCI specimens revealing the presence of the typical micro-shrinkage pores.

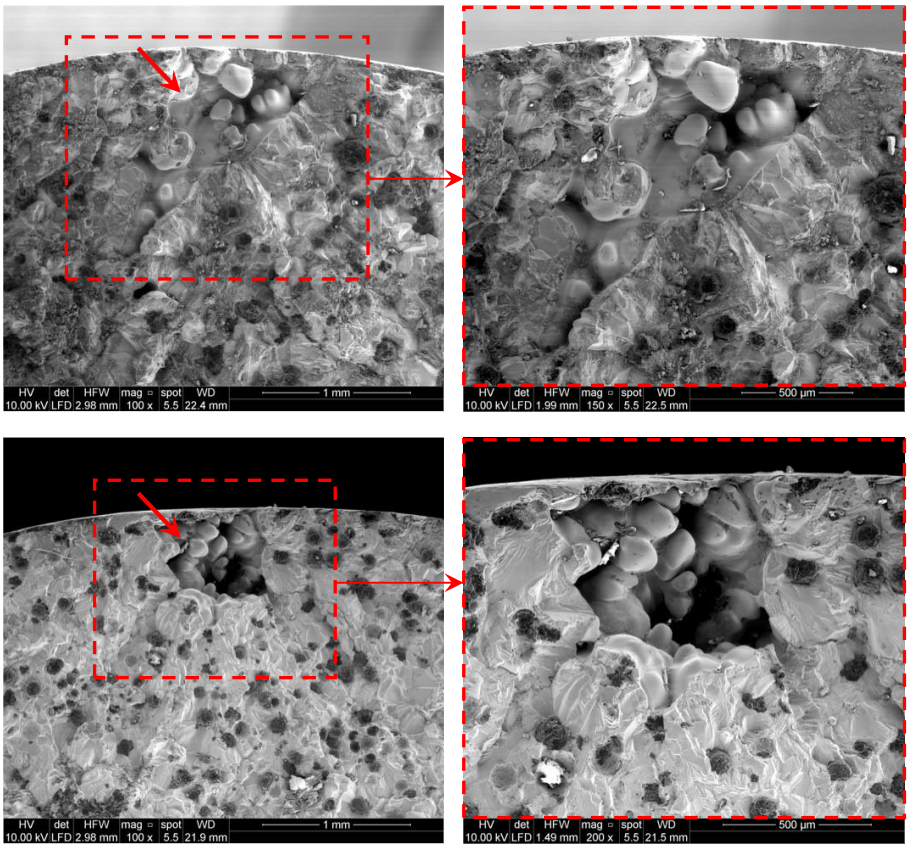

Figure 1. DCI SEM fracture surface analysis: micro-shrinkage pores at different magnification levels.

Therefore, in order to design heavy section DCI components against fatigue failure, the detrimental effect of such defects on fatigue strength has to be taken into account in fatigue assessment. One of the most employed approach is the $\sqrt{area}$-parameter model, proposed by Murakami[6] and Yanase et al.[7]. More precisely, several Authors have implemented the $\sqrt{area}$-parameter model in their proposed fatigue strength criteria, in order to improve fatigue strength/lifetime estimation (see for instance Refs **[4,8]**).

In such a context, the aim of the present paper is to theoretically investigate the fatigue behaviour of a DCI containing solidification defects, in terms of micro-shrinkage porosity. In particular, infinite life fatigue tests, available in the literature[9,10] and related to both uniaxial and biaxial cyclic loading, are hereafter simulated by means of a procedure for fatigue strength assessment[11], implementing:

(i) a statistical method deriving from Extreme Value Theory (EVT) to perform the defect content analysis;

(ii) the $\sqrt{area}$-parameter model[6,7] to compute the fatigue limits under normal and shear uniaxial cyclic loading;

(iii) the multiaxial critical plane-based criterion by Carpinteri at al.[12-17] for both the fatigue strength assessment and the estimation of the fracture plane orientation.

The above procedure has been originally applied to fatigue data related to a high strength steel containing non-metallic inclusions, providing satisfactory results in terms of fatigue strength estimations. More details regarding the analytical formulation of the present procedure can be found in Ref. **[11]**.

It is worth noticing that, although the experimental data here examined[9,10] have been already simulated by using the Carpinteri at al. criterion[15,16] (that is, without taking into account the effect of the shrinkage porosity), providing quite satisfactory results, a procedure taken into account the presence of such defects in the material is needed to be applied, being experimentally proved that the porosity area is the main cause of failure under high-cycle fatigue[9,10].

The present work is structured as follows. **Section 2** briefly summarises the state of the art on solidification defects and their influence on the mechanical and fatigue properties of DCI components. In **Section 3**, the framework of the procedure here employed for fatigue strength assessment and fracture plane determination is briefly presented. The experimental campaign examined, performed on DCI specimens containing solidification defects in terms of micro-shrinkage porosity and subjected to uniaxial and multiaxial fatigue loading, is described in detail in **Section 4**. In **Section 5** the above procedure is applied to the above experimental tests, whereas the results obtained are presented and discussed in **Section 6**. Finally, the main relevant conclusions are reported in **Section 7**.

2. SOLIDIFICATION DEFECT INFLUENCE ON MECHANICAL PROPERTIES: A BRIEF REVIEW

The most common solidification defects contained in heavy section DCI components are represented by non-nodular graphite elements (such as exploded, spiky and chunky graphite), non-metallic inclusions, slag inclusions, macro- and micro-shrinkage porosity and micro-pores related to the presence of gas[18]. Such defects, which have a detrimental effect on the mechanical properties of DCIs (both static and cyclic), can be partially avoided by means of some optimisation strategies[19,20], although their presence are unavoidable. Alonso et al.[20] have recently investigated the effect of selenium additions on the formation process of graphite, proving the substantial reduction of the solidification defects. Special nano-carbon additives have been used in the experimental research work by Ahmed et al.[21] in order to promote the tendency of spheroidal graphite formation.

As far as the *static properties* are concerned, the increase of non-nodular graphite content strongly decreases the mechanical properties of heavy section DCI components[3,22]. As reported in the interesting literature review by Källbom[23], the tensile strength and the elongation were strongly reduced due to the presence of chunky graphite in DCI microstructure, whereas the yield strength and hardness were not influenced. Moreover, also macro- and micro-shrinkage porosity affects the static properties of DCI components. For instance, Wang et al.[24] demonstrated that the tensile strength linearly decreased with the increasing of porosity areas, whereas the elongation at fracture sharply decreased.

Regarding the *fatigue properties* of thick walled DCI components, Čanžar and co-workers[25] experimentally proved that the fatigue crack nucleation and propagation process strongly depended on the size, shape and distribution of graphite particles. In particular, it was shown that the largest irregular graphite particles reduced both the fracture toughness and the fatigue strength. However, according to Borsato et al.[26], the fatigue behaviour is influenced mostly by micro-shrinkage porosity and less by degenerated graphite particles. Such a statement has been confirmed by several Authors. For instance, Nadot et al.[27,28], investigating the High Cycle Fatigue (HCF)

behaviour of a DCI under tensile cyclic loading, identified as crack nucleation site a single micro-shrinkage pore located at the specimen surface and, consequently, concluded that the solidification defects near the surface were more deleterious than the internal ones. Similarly, Kainzinger et al.[29] observed that micro-shrinkage pores were the dominant sites for fatigue crack nucleation in specimens extracted from a wind turbine hub made of DCI. Moreover, under tension-compression cyclic loading, the fatigue crack nucleation process in ferritic-pearlitic DCI specimens was considerably accelerated by the presence of micro-shrinkage pores near the specimen sub-surface, according to the experimental evidences reported in Ref. **[30]**. Similar results have been obtained also by Borsato et al.[31,32] regarding the fatigue behaviour of heavy section pearlitic DCI components. Furthermore, they argued that a combined effect between micro-shrinkage pores and non-nodular graphite particles could exist if they were both present in the DCI.

From the above discussion, it is clear that the effect of solidification defects on fatigue properties of DCI components has been thoroughly investigated. However, it is worth noting that this research topic is still open, since a unique approach regarding the influence of both non-nodular graphite particles and micro-shrinkage porosity on fatigue behaviour has not yet been achieved[33,34].

3. A PROCEDURE FOR FATIGUE STRENGTH ASSESSMENT OF METALS CONTAINING SOLIDIFICATION DEFECTS

The procedure, originally proposed for the fatigue strength assessment of metals containing inclusions[11] and here employed to take into account the presence of micro-shrinkage porosity, implements: (i) a statistical method deriving from EVT[35,36], (ii) the $\sqrt{area}$-parameter model[6,7], and (iii) the multiaxial critical plane-based criterion by Carpinteri at al.[12-17]. The flowchart of the procedure is reported in **Ref. [11]**.

The algorithm requires some *input data* related to: the applied loading conditions (ranges of both normal, $\Delta\sigma$, and shear, $\Delta\tau$,

stresses applied to the specimen, the phase angle, β, between the normal stress and the shear stress, and the loading ratio, R); the mechanical properties of the material (the ultimate tensile strength, σ_u, and the Vickers hardness, HV); the values of the volumes $V_{0,n}, V_{0,s}, V$ and V_{max}, being, respectively, the standard inspection volumes related to normal and shear uniaxial cyclic loading, the volume of the useful cross-section (prediction volume) and its maximum value.

A statistical method deriving from EVT[35,36] is used to obtain the distribution of defects and the return period related to both normal (T_n) and shear (T_S) uniaxial cyclic loading. More precisely, to such an aim the fracture surface of specimens, under both normal and shear uniaxial cyclic loading, are examined and the values of $\sqrt{area_n}_{max}$ and $\sqrt{area_s}_{max}$ (representing the square root of the expected maximum size of the defect for each of the above loading conditions) are determined.

Once the $\sqrt{area_n}_{max}$ and $\sqrt{area_s}_{max}$ are computed, the *fatigue limits under normal loading*, σ_w, and *shear loading*, τ_w, of the material are calculated by means of the $\sqrt{area}$-parameter model[6,7].

Under normal cyclic loading, Murakami[35,36] suggested that the value of σ_w could be calculated as a function of both the material Vickers hardness, HV, and the $\sqrt{area_n}_{max}$, by means of the following equation:

$$\sigma_w = \frac{1.41\left(HV + 120\right)}{\left(\sqrt{area_n}_{max}\right)^{1/6}} \qquad \textbf{(1)}$$

It is worth noticing[6] that the above equation is related to a defect just below the cross-section surface and corresponding to a number of loading cycles equal to $1 \cdot 10^7$.

By following the Murakami proposal, Yanase et al.[7] formulated a similar relationship for the computation of the fatigue limit under shear loading, τ_w, that is:

$$\tau_w = \frac{1.19\left(HV + 120\right)}{\left(\sqrt{area_s}_{max}\right)^{1/6}} \quad \textbf{(2)}$$

Once the fatigue limits are computed, the *fatigue strength assessment of the material* is performed for each simulated test, according to the Carpinteri et al. criterion[12-17].

More precisely, firstly the orientation of the critical plane (that is, the verification plane where the fatigue strength is performed) is determined. Such an orientation, which is assumed to be dependent on the averaged directions $(\hat{1},\hat{2},\hat{3})$ of the principal stress axes, is hence defined by means of an off-angle δ formed by w-direction (i.e. the direction normal to the critical plane) and $\hat{1}$ (i.e. the averaged direction of the maximum principal stress, assumed corresponding to the normal to the fracture plane) in the plane $\hat{1}\hat{3}$:

$$\delta = \frac{3\pi}{8}\left[1 - \left(\frac{\tau_w}{\sigma_w}\right)^2\right] \quad \textbf{(3)}$$

Note that in the Carpinteri et al. criterion[12-16], the fatigue limits σ_w (Eq.(1)) and τ_w (Eq.(2)), here employed in Eq. (3), are replaced by the experimental fatigue strengths (at a given number of loading cycles) for fully reversed normal stress, $\sigma_{af,-1}$, and for fully reversed shear stress, $\tau_{af,-1}$, respectively.

Then, the fatigue endurance condition is posed by equating the amplitude of an equivalent uniaxial stress, $\sigma_{eq,a}$, to the normal fatigue strength, σ_w, that is:

$$\sigma_{eq,a} = \sqrt{N_{eq,a}^2 + \left(\frac{\sigma_w}{\tau_w}\right)^2 C_a^2} = \sigma_w \quad \textbf{(4)}$$

with:

$$N_{eq,a} = N_a + \sigma_w\left(\frac{N_m}{\sigma_u}\right) \quad \textbf{(5)}$$

In particular, N_a and N_m are, respectively, the amplitude and the mean value of the normal component, $\mathbf{N}$, of the stress vector, $\mathbf{S_w}$,

on the critical plane, whereas C_a is the amplitude of the shear component, $\mathbf{C}$, of $\mathbf{S_w}$.

Finally, the error index, I, is computed for each simulated test:

$$I = \frac{\sigma_{eq,a} - \sigma_w}{\sigma_w} \cdot 100 \quad \textbf{(6)}$$

The described procedure is repeated, and consequently the algorithm executed, by varying the value of V up to the value V_{max}, in order to determine the optimised return period $T_n = T_{opt}$, as detailed in **Section 5.1.3.**

4. THE EXPERIMENTAL CAMPAIGN EXAMINED

The experimental campaign, hereafter simulated through the procedure presented in **Section 3**, can be found in the literature[9,10]. In particular, the material was a DCI characterised by uniformed distributed spheroidal graphite particles (produced with the addition of minor elements such as magnesium, calcium, cerium) and a fully pearlitic matrix. According to the European designation, it is named DCI EN-GJS-700-2: its ultimate tensile strength is equal to 689 MPa[37] and its Vickers hardness is equal to 298 $\mathrm{kg_f/mm^2}$[38]. The chemical composition of such a DCI consisted in: 2.90-3.70 C, 1.50-2.20 Si, 0.10-0.70 Mn, 0.10-0.60 Cr, 1.90-2.90 Ni and 0.30-0.90 Mo (by weight %).

The experimental campaign referred to infinite fatigue life tests, that is the number of loading cycles to failure was mostly greater than $1 \cdot 10^5$ cycles. In particular, small cylindrical specimens, cut from DCI large section, were subjected to both uniaxial (tension or torsion) and biaxial (combined compression and torsion) cyclic loading with a constant amplitude. Tensile fatigue tests were performed under load control on specimens with a gauge section diameter of 7 mm, by means of a Rumul machine; torsional and biaxial fatigue tests were conducted under load control on specimens characterised by a gauge section diameter of 16 mm and a multiaxial servohydraulic test system was used. Both uniaxial and biaxial

fatigue loadings were applied according to the staircase method, as reported in detail in Ref. **[9]**.

The uniaxial fatigue tests were characterised by a loading ratio, R, equal to -1. As far as biaxial tests are concerned, the axial loading was always in compression with a mean value different from zero, whereas the torsional loading was fully reversed and a phase shift, β, between axial and torsional loading of 90° was considered.

The uniaxial and biaxial fatigue data are listed in **Tables 1** and **2**, respectively, where the symbols σ_a and τ_a represent the amplitude of the applied normal and shear stresses. The experimental number of loading cycles to failure, N_{exp}, is also reported in the above Tables. Note that, the run-out condition was assumed when a specimen survived more than $1 \cdot 10^7$ cycles, whereas the failed condition was usually defined when the crack was visually observed during the test.

From the uniaxial fatigue data, the fully reversed normal and shear fatigue limits were computed by using the up- and -down method proposed in Ref. **[39]**, and more precisely: $\sigma_{af,-1} = 197\,\text{MPa}$ and $\tau_{af,-1} = 178\,\text{MPa}$.

After fatigue testing, all specimens were cut in order to observe the fracture surfaces for each loading condition being examined, and more precisely:

- under tensile cyclic loading, the fracture surfaces were flat and perpendicular to the specimen longitudinal axis (that is, perpendicular to the maximum principal stress direction);
- under torsional cyclic loading, the fracture surfaces were at 45° with respect to the specimen longitudinal axis;
- under biaxial cyclic loading, the fracture surfaces were both flat and 45°.

Table 1. Uniaxial fatigue data related to the experimental campaign examined **[9,10]**.

TEST No.	σ_a [MPa]	σ_m [MPa]	τ_a [MPa]	τ_m [MPa]	$\sqrt{area_{n\ j}}$ [μm]	N_{exp} [cycles]	
1	260	0			866	$2.46 \cdot 10^6$	Failed
2	240	0			265	$1.00 \cdot 10^7$	*Run-out*

3					1000	$1.39 \cdot 10^6$	Failed
4	220	0			418	$7.29 \cdot 10^5$	Failed
5	200	0			1077	$8.09 \cdot 10^6$	Failed
6					980	$2.03 \cdot 10^5$	Failed
7	180	0			1158	$4.18 \cdot 10^6$	Failed
8					366	$1.00 \cdot 10^7$	*Run-out*
9	160	0			1183	$2.72 \cdot 10^6$	Failed
10					2552	$1.00 \cdot 10^7$	*Run-out*
11	140	0			1162	$1.00 \cdot 10^7$	*Run-out*
12			190	0	NA	$9.76 \cdot 10^5$	Failed
13					NA	$8.80 \cdot 10^5$	Failed
14					NA	$7.77 \cdot 10^5$	Failed
15					NA	$1.66 \cdot 10^6$	Failed
16			165	0	NA	$1.00 \cdot 10^7$	*Run-out*
17					NA	$1.00 \cdot 10^7$	*Run-out*
18					NA	$1.00 \cdot 10^7$	*Run-out*

Table 2. Biaxial fatigue data related to the experimental campaign examined **[9,10].**

TEST No.	σ_a [MPa]	σ_m [MPa]	τ_a [MPa]	τ_m [MPa]	β [°]	N_{exp} [cycles]	
19	300	-300	150	0	90	$1.34 \cdot 10^6$	Failed
20	250	-250	125	0	90	$1.00 \cdot 10^7$	Failed
21						$9.11 \cdot 10^5$	Failed
22						$3.91 \cdot 10^6$	Failed
23						$2.71 \cdot 10^6$	Failed
24	225	-225	150	0	90	$9.93 \cdot 10^5$	Failed
25						$1.12 \cdot 10^6$	Failed
26						$1.40 \cdot 10^6$	Failed
27	200	-200	100	0	90	$1.00 \cdot 10^7$	*Run-out*
28						$9.32 \cdot 10^6$	Failed
29						$1.00 \cdot 10^7$	*Run-out*
30						$1.00 \cdot 10^7$	*Run-out*
31	187.5	-187.5	125	0	90	$1.00 \cdot 10^7$	*Run-out*
32						$5.94 \cdot 10^6$	Failed
33						$2.58 \cdot 10^6$	Failed
34						$1.00 \cdot 10^7$	*Run-out*
35	150	-150	100	0	90	$1.00 \cdot 10^7$	*Run-out*
36	150	-150	75	0	90	$1.00 \cdot 10^7$	*Run-out*

Subsequently, the surfaces of all the broken specimens were examined by using Scanning Electron Microscope (SEM), noting that fatigue cracks usually nucleated in correspondence of the largest solidification defect, i.e. the largest micro-shrinkage pore. Such cracks, after propagation, led to the fatigue failure of the specimens.

Only for the tensile fatigue tests, the Authors measured the largest micro-shrinkage pores of each specimen. More precisely, for each specimen, after manual drawing the edges of such pores on the SEM image, a commercial software was used to measure the square root of such defect areas. Then, for each specimen the maximum value is computed as reported in the original work by Cengiz[9], and here listed as $\sqrt{area_n}_j$ in **Table 1.**

5. PROCEDURE APPLICATION

The procedure presented in **Section 3** is hereafter employed to simulate the experimental data presented in **Section 4.**

5.1 Defect content analysis by means of a statistical method deriving from EVT

The defect content analysis is performed, according to a statistical method deriving from EVT[11,35,36,40], by employing the experiment data $\sqrt{area_n}_j$ listed in **Table 1.** More precisely, the analysis is performed on data related to normal uniaxial cyclic loading, and the result is extended to the case of shear uniaxial cyclic loading, that is: $\sqrt{area_s}_{max} = \sqrt{area_n}_{max}$ (i.e. $T_n = T_s$).

Firstly, the distribution of defects is determined; then, the return period, T_n, is computed; finally, the value of the $\sqrt{area_n}_{max}$, that is the square root of the expected maximum size of the defect related to normal loading, is calculated. Moreover, also an optimised T_n value is computed by exploiting a relationship, here proposed to optimise the accuracy of the procedure in terms of fatigue strength estimation.

5.1.1 Distribution of defects

Let us consider the experimental data $\sqrt{area_n}_j$ (**Table 1**).

Firstly, such values are classified in ascending order, and then indexed with $j=1,\ldots,k$, being k the number of the examined tensile fatigue data (i.e. $k=11$):

$$\sqrt{area_n}_1 \le \sqrt{area_n}_2 \le \cdots \le \sqrt{area_n}_{11} \quad \textbf{(7)}$$

Then, the reduced variable, y_j, is calculated as follows:

$$y_j = -\ln\left[-\ln\left(\frac{j}{11+1}\right)\right] \quad \textbf{(8)}$$

The probability graph of the defect distribution is plotted in **Figure 2**, where the y_j values are reported on the ordinate axis, whereas the $\sqrt{area_n}_j$ values are reported on the abscissa axis.

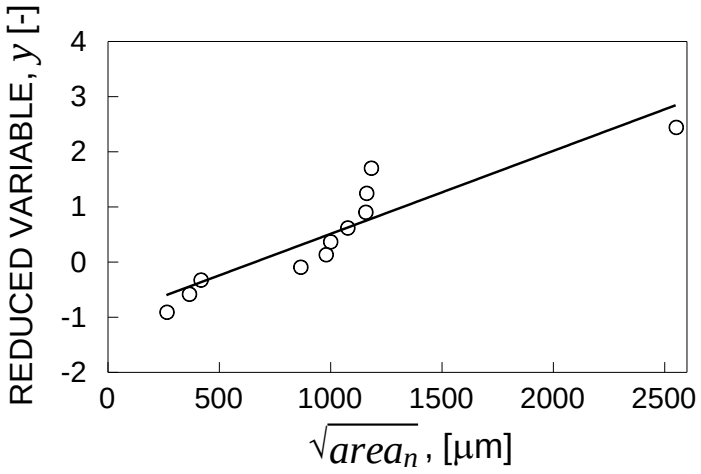

Figure 2. Probability graph of the defect distribution according to the extreme value theory.

From **Figure 2** it can be observed that the reduced variable y against the $\sqrt{area_n}$ has a linear trend, that is, such points follow a Gumbel distribution. The linear regression of the above defect distribution is given by:

$$\sqrt{area_n}_{max} = \frac{1}{0.0015} y_n + \frac{1.0095}{0.0015} \quad \textbf{(9)}$$

with:

$$y_n = -\ln\left[-ln\left(\frac{T_n - 1}{T_n}\right)\right] \quad \textbf{(10)}$$

being T_n the return period related to normal uniaxial cyclic loading.

5.1.2 The return period

From Eq.(9), it can be noted that the $\sqrt{area_n}_{max}$ value is a function of the return period, T_n. However, in order to define the T_n value, some remarks are needed. In particular, the solidification defects (i.e. the micro-shrinkage pores) are distributed in a three-dimensional region and, consequently, the $\sqrt{area}_{max}$ value depends on the volume considered in the defect content analysis. As a matter of fact, the greater the volume considered, the greater the probability of finding larger defects within such a volume. Therefore, the return period, T_n, is defined as the ratio of two volumes, and more precisely:

$$T_n = \frac{V}{V_{0,n}} \tag{11}$$

being V the prediction volume and $V_{0,n}$ the standard inspection volume related to normal uniaxial cyclic loading.

Note that, V is usually set equal to the volume of the specimen gauge region, whereas $V_{0,n}$ is computed by assuming a given thickness, h_n, associated to the inspection area S_0 [6,11,35,36,40], that is:

$$V_{0,n} = S_0 h_n \tag{12}$$

with:

$$h_n = \frac{\sum_j^{11} \sqrt{area_n}_j}{11} \tag{13}$$

Once T_n is computed, the $\sqrt{area_n}_{max}$ value is calculated through Eqs (9) and (10).

In the present study, the value of the standard inspection volume, $V_{0,n}$, turns to be equal to $39.10\,\text{mm}^3$, being $S_0 = 39\,\text{mm}^2$ [10] and $h_n = 1.00\,\text{mm}$.

Regarding the useful cross-section volume, V, different values are here considered in order to optimise the accuracy of the procedure in terms of fatigue strength estimation.

5.1.3 The optimised return period

The first value of T_n considered (indicated as T_n^* in **Table 3**) is that derived from the $\sqrt{area_n}_{max}$ value reported by the Authors of Refs **[9,10]**, that is $\sqrt{area_n}_{max} = 1161.97 \mu m$. From such a value, $y_n = 0.73$ and $T_n^* = 2.62$ are computed by means of Eqs (9) and (10), respectively.

Then, three other values of V (that is, three other values of T_n) are assumed by considering different values of the gauge length, L_0. However, due to the fact that the value of L_0 for tensile fatigue specimens is not available in Refs **[9,10]**, it is hereafter defined as a multiple of the gauge section diameter, d, according to the most relevant standards. In particular, by assuming $L_0 = d, 2d, 3d$, the corresponding gauge region volumes and return periods turn to be equal to: $V_1(L_0 = d) = 134.70\,\text{mm}^3$ and $T_{n,1} = 3.45$, $V_2(L_0 = 2d) = 538.78\,\text{mm}^3$ and $T_{n,2} = 13.78$, $V_3(L_0 = 3d) = 808.17\,\text{mm}^3$ and $T_{n,3} = 20.67$ (see **Table 3**).

Moreover, the return period corresponding to the experimental fatigue limit $\sigma_{af,-1} = 197\,\text{MPa}$ is derived, and listed in **Table 3**.

For each of the above values of T_n, the fatigue limits σ_w and τ_w are computed through Eqs (1) and (2) and listed in **Table 3**, by assuming $\sqrt{area_s}_{max} = \sqrt{area_n}_{max}$ for each value of V examined, that is $T_n = T_s$.

The block of the Carpinteri et al. criterion in the algorithm is executed and the corresponding mean value of the error index, $\bar{I}$ (computed by considering all the simulated experimental tests), is determined for each of the above T_n values. The maximum value of V adopted is $V_{max} = 808.17\,\text{mm}^3$.

Table 3. Return period, useful cross-section volume, fatigue limits and error index mean value corresponding to the simulations performed.

T_n		V	σ_w	τ_w	$\bar{I}$
Symbol	Value	[mm^3]	[MPa]	[MPa]	[%]
T_n^*	2.62	102.51	185.64	153.41	-4.27
$T_{n,1}$	3.45	134.70	180.25	148.96	-1.40
$T_{n,2}$	13.78	538.78	164.54	135.97	8.02
$T_{n,3}$	20.67	808.17	161.72	133.50	10.02
Exp. camp.	1.80	70.44	197.00	178.00	-12.05
T_{opt}	5.37	209.79	173.80	143.63	0.00

Now, the mean value of the error index, $\bar{I}$, is plotted against the return period T_n, as shown in **Figure 3**. By interpolating the above points with a logarithmic curve, the following relationship is obtained (R-squared = 0.944757):

$$\bar{I}(T_n) = 8.225 \ln(T_n) - 13.818 \quad (14)$$

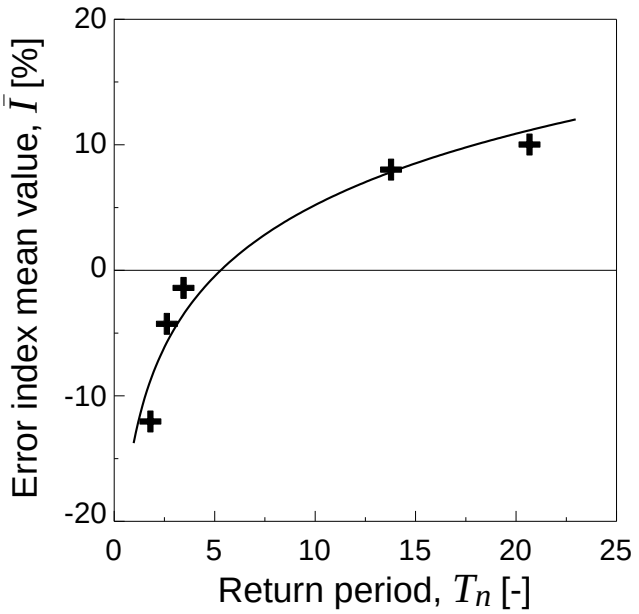

Figure 3. Error index mean value vs. return period.

From Eq.(14), it is possible to derive the value of T_n for which $\bar{I} = 0$, i.e. $T_{opt} = 5.37$. Consequently, by exploiting Eqs (9) and (10), the value of $\sqrt{area_n}_{max} = 1725.51 \mu m$ is computed, and the fatigue limits

σ_w and τ_w are calculated (see **Table 3**). The block named Carpinteri et al. criterion in the algorithm is executed for the last time.

6. RESULTS AND DISCUSSION

In the present Section, the results in terms of both fatigue strength and fatigue fracture plane determined by applying the present procedure (**Section 3**) are shown and compared to the experimental ones described in **Section 4**. In particular, the uniaxial and biaxial fatigue data related to DCI EN-GJS-700-2[9,10] are here analysed by considering the fatigue limits corresponding to $T_{opt}=5.37$, that is $\sigma_w=173.80\text{MPa}$ and $\tau_w=143.63\text{MPa}$.

6.1 Fatigue strength assessment

The results in terms of stress components on the critical plane (i.e. $N_{eq,a}$ and C_a) are listed in **Table 4** for tensile loading (tests No. 1-11), torsional loading (tests No. 12-18) and biaxial loading (tests No. 19-36). Note that, for tests performed at the same stress level (for instance, tests No. 2 and 3), the present procedure is able to provide only one pair of values $N_{eq,a}$-C_a.

The above results in terms of stress components are plotted in **Figures 4(a), 5(a) and 6(a)** for all data being examined (that is, each point corresponds to a given experimental test). In the above $N_{eq,a}$-C_a plot, the fatigue endurance condition, given by Eq. (4), defines an ellipse with the semi-axes equal to σ_w along the abscissa and to τ_w along the ordinate. The dashed lines in the above Figures correspond to an error band equal to $\pm 20\%$.

Note that, if the $N_{eq,a}$-C_a point lies inside the above ellipse, a run-out condition is predicted by the present criterion; whereas, fatigue failure is estimated if the $N_{eq,a}$-C_a point is outside the elliptical domain. Moreover, if both run-out and failure conditions were experimentally observed (see tests No. 2-3, 7-8 and 9-10 in **Table 1**, and tests No. 27-30 and 31-34 in **Table 2**), only one of the

above condition can be provided by the applied procedure. In particular, in order to obtain conservative results, the fatigue failure condition should be estimated.

Table 4. Results in terms of stress components on the critical plane.

TEST No.	$N_{eq,a}$ [MPa]	C_a [MPa]
1	225.39	88.33
2-3	208.05	81.53
4	190.71	74.74
5-6	173.37	67.94
7-8	156.04	61.15
9-10	138.70	54.35
11	121.36	47.56
12-15	139.42	129.10
16-18	121.08	112.11
19	42.68	150.03
20-23	35.57	125.02
24-26	54.30	145.42
27-30	28.45	100.02
31-34	45.25	121.19
35	36.20	96.95
36	21.34	75.01

As far as uniaxial fatigue data are concerned, the following remarks can be made:

- for tensile fatigue loading (**Figure 4(a)**), the experimental failure (tests No. 1, 4, 5-6) and run-out (test No. 11) conditions are perfectly predicted by means of the present procedure. For experimental tests, which showed both failures and run-outs, the procedure provides conservative estimations for tests No. 2-3 and 7-8 (being the $N_{eq,a}$-C_a points outside or on the ellipse) and not for tests No. 9-10;
- for torsional fatigue loading (**Figure 5(a)**), the procedure estimates fatigue failure for tests No. 12-15 in agreement with the experimental outcomes, whereas a condition of incipient failure is obtained for tests No. 16-18 (that is, the corresponding $N_{eq,a}$-C_a

point lies very close to the failure curve), even if run-outs were observed.

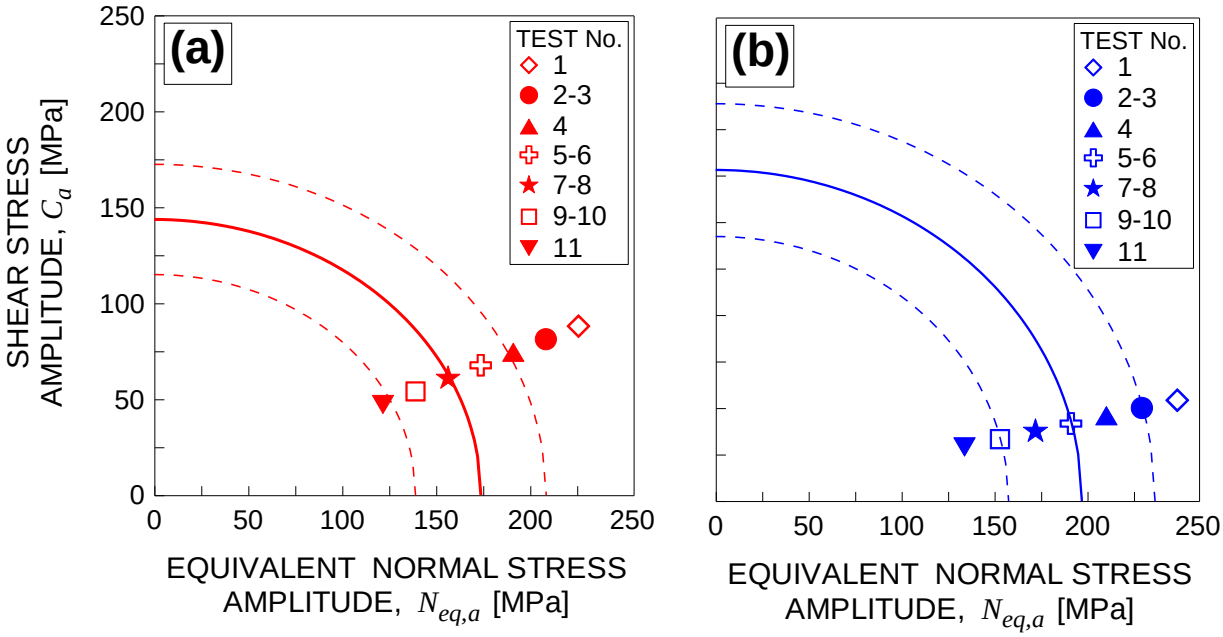

Figure 4. Shear stress amplitude vs equivalent normal stress amplitude for *tensile fatigue tests*, according to the: (a) present procedure and (b) Carpinteri et al. criterion.

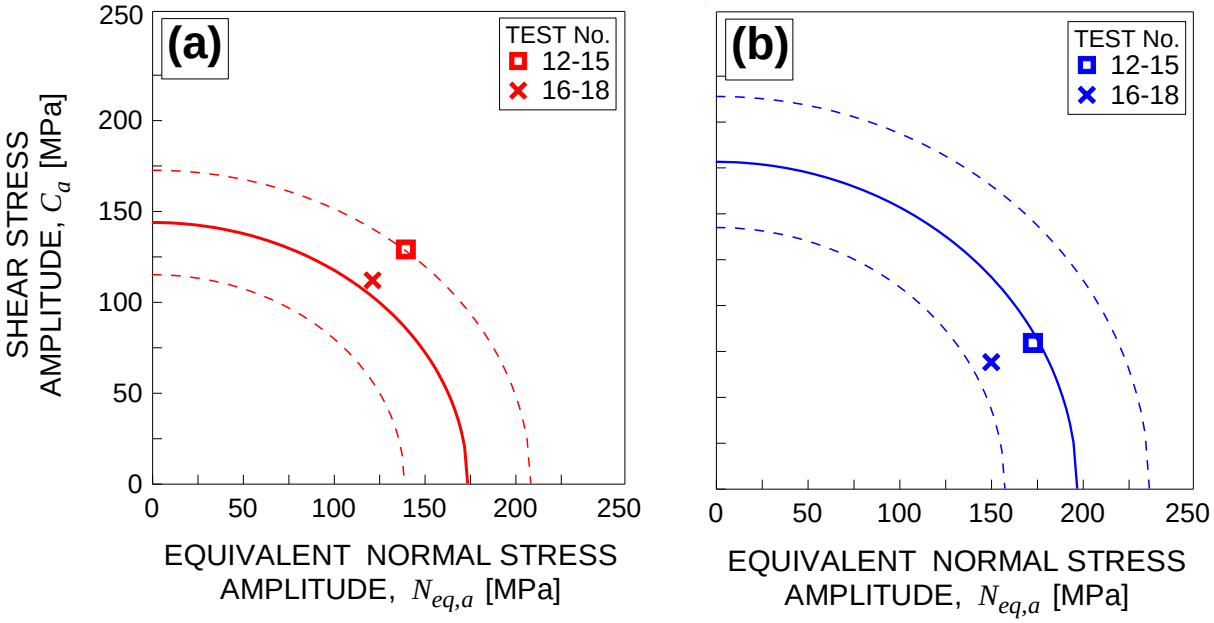

Figure 5. Shear stress amplitude vs equivalent normal stress amplitude for *torsional fatigue tests*, according to the: (a) present procedure and (b) Carpinteri et al. criterion.

From **Figure 6(a)** related to biaxial fatigue loading, it can be observed that:

- the present procedure allows to correctly estimate the failure of the specimens for tests No. 19 and 24-26 and the run-out condition for tests No. 35 and 36;
- for experimental tests characterised by both failures and run-out (that is, tests No. 27-30 and 31-34), the procedure provides non-conservative results since the $N_{eq,a}$-C_a points are located inside the elliptical domain;
- for tests No. 20-23, the experimental failure condition is not captured by means of the present procedure.

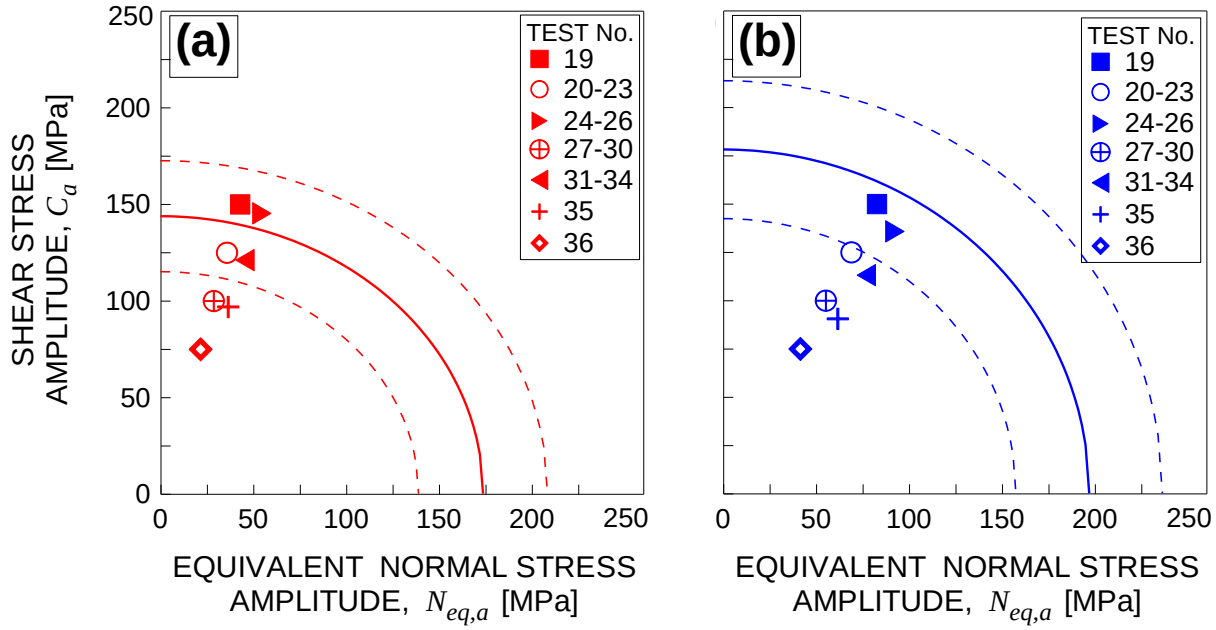

Figure 6. Shear stress amplitude vs equivalent normal stress amplitude for *biaxial fatigue tests*: according to the: (a) present procedure and (b) Carpinteri et al. criterion.

Note that, even if the procedure provides non-conservative results for tests No. 9-10, 27-30 and 31-34, the obtained results fall into or close to the scatter band equal to -20%, proving the accuracy of the present estimations.

In order to assess the effectiveness of the present procedure, the above theoretical results are also compared with those derived through the Carpinteri et al. criterion. In particular, such results in terms of $N_{eq,a}$-C_a are reported in **Figures 4(b)**, **5(b)** and **6(b)**. From **Figures 4-6**, it can be observed that the original formulation

of the Carpinteri et al. criterion is not able to correctly predict the experimental failures for tests No. 5-6, 12-15, 19 and 24-26, unlike the present procedure. Moreover, the Carpinteri et al. criterion provides in general much more non-conservative results with respect to those obtained by applying such a procedure.

Let us consider only the tests in **Table 3** that show failure conditions. For such tests, the equivalent stress amplitude computed according to both the present procedure and the Carpinteri et al. criterion is plotted in **Figure 7**. The horizontal thick lines represent the fatigue limit $\sigma_w = 173.80\,\text{MPa}$ (line in red) and the fatigue limit under fully reversed normal stress $\sigma_{af,-1} = 197\,\text{MPa}$ (line in blue). It can be observed that when the present procedure is applied to the above experimental data, 86% of the fatigue strength estimations are conservative, whereas only the 29% of the estimations are conservative when the Carpinteri et al. criterion is applied.

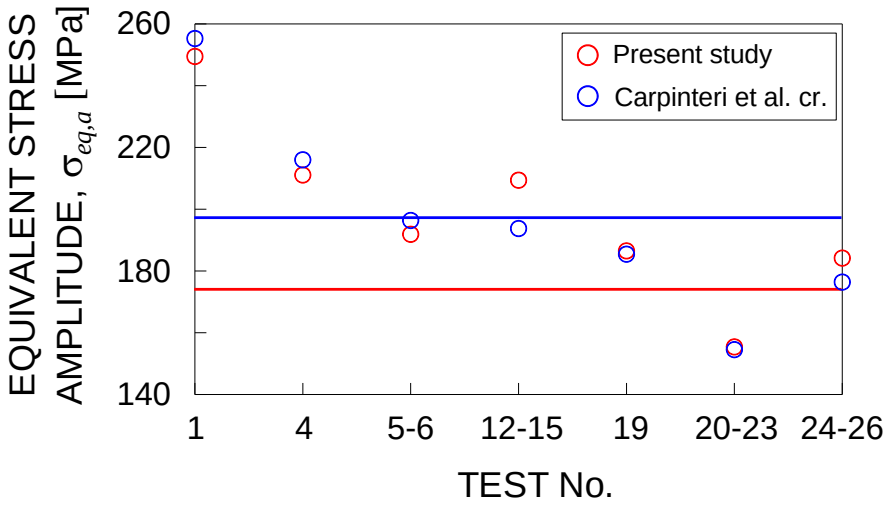

Figure 7. Equivalent stress amplitude against the test No., computed according to both the present procedure and the Carpinteri et al. criterion.

It can be pointed out that for materials containing defects (such as the present DCI), most accurate results are obtained when the influence of such defects on fatigue strength is taken into account in the fatigue strength assessment.

6.2 Fracture plane prediction

The results in terms of fracture plane orientation (i.e. θ_{cal}) are listed in **Table 5** for tensile loading (tests No. 1-11), torsional loading (tests No. 12-18) and biaxial loading (test No. 19-36). Moreover, also the experimental values of fracture plane orientation, θ_{exp} [9,10], (see **Section 4**) are reported in **Table 5**.

Table 5. Results in terms of both experimental, θ_{exp} [9,10], and theoretical fracture plane orientation, θ_{cal}.

TEST No.	θ_{exp} [°]	θ_{cal} [°]
1	90.0	90.0
2-3	90.0	90.0
4	90.0	90.0
5-6	90.0	90.0
7-8	90.0	90.0
9-10	90.0	90.0
11	90.0	90.0
12-15	45.0	45.0
16-18	45.0	45.0
19	90.0 – 45.0	29.9
20-23	90.0 – 45.0	29.9
24-26	90.0 – 45.0	32.3
27-30	90.0 – 45.0	29.9
31-34	90.0 – 45.0	32.3
35	90.0 – 45.0	32.3
36	90.0 – 45.0	29.9

Note that, tests performed at the same stress level are represented, according to the present procedure, by only one value of θ_{cal}. In particular, the orientation of the fracture plane is derived from the direction cosine of the averaged direction $\hat{1}$ (that is, the normal to fatigue fracture plane) with respect to the longitudinal axis of the specimen.

From **Table 5**, it can be observed that:

(a) for tensile fatigue loading, the procedure estimates, for all the examined tests, a fracture plane orientation, θ_{cal}, equal to $90°$

(that is, perpendicular to the specimen axis), totally in agreement with the experimental outcomes;

(b) for torsional fatigue loading, the procedure provides, for all the examined tests, a fracture plane with a θ_{cal} orientation of $45°$ with respect to the specimen axis, totally in agreement with the experimental outcomes;

(c) for biaxial fatigue loading, the orientation of the fracture plane, θ_{cal}, turns out to be equal to about $30°$ for tests No. 19, 20-23, 27-30, 36 and to about $32°$ for tests No. 24-26, 31-34, 35. Note that, in such a case, only one of the two experimental fracture plane orientations can be predicted by means of the present procedure. In particular, the θ_{exp} orientation inclined with respect to the specimen axis is capture by means of the present procedure.

7. CONCLUSIONS

In the present paper, the fatigue behaviour of a DCI containing solidification defects in terms of micro-shrinkage porosity has been analysed by using a fatigue strength assessment procedure, implementing: (i) a statistical method deriving from EVT, (ii) the $\sqrt{area}$-parameter model, and (iii) the multiaxial critical plane-based criterion by Carpinteri at al.

The defect content analysis on the experimental data related to specimens under cyclic tensile loading has been performed, taking into account all the tested specimens, in contrast to the common practical use to consider only a single specimen. Moreover, the return period, $T_n = T_{opt}$, has been computed by a suitable relationship, in order to equate to zero the average value of the error index.

By using such a return period, named optimised return period, the fatigue limits under normal and shear loadings have been computed.

The fatigue strength assessment of the DCI examined has been performed, showing a quite accurate estimation of experimental both failure and run-out. More precisely, according to the present procedure, the fatigue strength estimation is more conservative with

respect to that predicted by the Carpinteri et al. criterion, in favour of safety.

Moreover, by means of the present procedure it is possible to achieve a quite good prediction of the fracture plane orientation for the examined experimental tests, especially for uniaxial fatigue loading. It is important to point out that, unlike many fatigue criteria available in the literature, such a procedure allows also to estimate the orientation of the crack initiation path, which is assumed coincident with the critical plane orientation.

In conclusion, the present procedure, where an optimised computation of the return period has been implemented, has shown to be able to correctly estimate not only the fatigue strength but also the fracture plane orientation of naturally defective materials. Therefore, such a procedure can be considered as a powerful engineering tool in fatigue design of real components. Finally, the great potential of this procedure is that the defect content analysis (performed by means of a statistical method deriving from EVT) can be easily performed by using machine learning techniques.

Acknowledgements

The work of Sabrina Vantadori and Andrea Zanichelli is supported by Italian Ministry of University and Research (P.R.I.N. National Grant 2017, Project code 2017HFPKZY; University of Parma Research Unit).

Author contributions

Sabrina Vantadori: Conceptualization, Supervision, Funding acquisition, Investigation, Writing
Camilla Ronchei: Formal analysis, Investigation, Writing
Daniela Scorza: Formal analysis, Investigation, Review & Editing
Andrea Zanichelli: Formal analysis, Investigation, Review & Editing
Raimondo Luciano: Supervision, Investigation, Review & Editing

REFERENCES

[1] Benedetti M, Curtolo T, Dallago M, Fontanari V, Lusuardi D. Yield and fracture loci for a ductile cast iron EN-GJS-600–3 under biaxial stresses. Fatigue Fract Eng Mater Struct. 2022;45: 783- 800.

[2] Hesseler J, Baumgartner J, Bleicher C. Consideration of the transient material behavior under variable amplitude loading in the fatigue assessment of nodular cast iron using the strain-life approach. Fatigue Fract Eng Mater Struct. 2021;44: 2845– 2857.

[3] Benedetti M, Torresani E, Fontanari V, Lusuardi D. Fatigue and Fracture Resistance of Heavy-Section Ferritic Ductile Cast Iron. Metals 2017;7: 88.

[4] Borsato T, Ferro P, Berto F. Novel method for the fatigue strength assessment of heavy sections made by ductile cast iron in presence of solidification defects. Fatigue Fract Eng Mater Struct. 2018;41: 1746–1757.

[5] Ferro P, Lazzarin P, Berto F. Fatigue properties of ductile cast iron containing chunky graphite, Mater. Sci. Eng. A 2012;554: 122-128.

[6] Murakami Y. Metal Fatigue: Effects of Small Defects and Nonmetallic Inclusions. Oxford, UK: Elsevier Science Ltd.; 2002.

[7] Yanase K, Endo M. Multiaxial high cycle fatigue threshold with small defects and cracks. Eng. Fract. Mech. 2014;123: 182–196.

[8] Yamabe J, Kobayashi M. Influence of casting surfaces on fatigue strength of ductile cast iron. Fatigue Fract. Eng. Mater. Struct. 2006;29: 403-415.

[9] Cengiz C. Out of phase multiaxial fatigue strength of a cast iron. Master thesis: Politecnico di Milano, Milan; 2012.

[10] Cristea ME, Foletti S, Cengiz C. Out of phase multiaxial fatigue strength of cast iron. In Proceedings of the Tenth International Conference on Multiaxial Fatigue & Fracture (ICMFF10), Kyoto (Japan), 2013.

[11] Scorza D, Carpinteri A, Ronchei C, Vantadori S, Zanichelli A. Effect of non-metallic inclusions on aisi 4140 fatigue strength. Int J Fatigue 2022, under review.

[12] Carpinteri A, Ronchei C, Scorza D, Vantadori S. Critical plane orientation influence on multiaxial high-cycle fatigue assessment. Phys. Mesomech 2015;18: 348-354.

[13] Vantadori S, Carpinteri A, Luciano R, Ronchei C, Scorza D, Zanichelli A, Okamoto Y, Saito S, Itoh T. Crack initiation and life estimation for 316 and 430 stainless steel specimens by means of a critical plane approach. Int J. Fatigue 2020;138: 105677.

[14] Ronchei C, Vantadori S. Notch fatigue life estimation of Ti-6Al-4V. Eng Fail Anal. 2021;120: 105098.

[15] Vantadori S, Ronchei C, Scorza D, Zanichelli A, Carpinteri A. Fatigue behaviour assessment of ductile cast iron smooth specimens. Int J Fatigue 2021;152: 106459.

[16] Vantadori S, Carpinteri A, Ronchei C, Scorza D, Zanichelli A, Fatigue strength evaluation and lifetime estimation for ductile cast irons under multiaxial loading. Procedia Struct Integr. 2021;33: 773-780.

[17] Vantadori S, Ronchei C, Scorza D, Zanichelli A, Araújo LC, Araújo JA Influence of non-metallic inclusions on the high cycle fatigue strength of steels. Int J Fatigue 2022;154: 106553.

[18] Skaland T. A new method for chill and shrinkage control in ladle treated ductile iron. In Keith Millis Symposium on Ductile Cast Iron, Hilton Head Island, SC, USA, 2003

[19] Borsato T, Berto F, Ferro P, Carollo C. Effect of in-mould inoculant composition on microstructure and fatigue behaviour of heavy section ductile iron castings. Procedia Struct Integr. 2016;2: 3150-3157.

[20] Alonso G, Stefanescu DM, Aguado E, Suarez R. The role of selenium on the formation of spheroidal graphite in cast iron. Metals 2021;11: 1600.

[21] Ahmed M, Soliman M, Youssef M, Bähr R, Nofal A. Effect of niobium on the microstructure and mechanical properties of alloyed ductile irons and austempered ductile irons. Metals 2021;11: 703.

[22] Di Cocco V, Iacoviello F, Cavallini M. Damaging micromechanisms characterization of a ferritic ductile cast iron. Eng Fract Mech 2010;77(11):2016–23.

[23] Kallbom R, Hamberg K, Björkegren LE. Chunky graphite—Formation and influence on mechanical properties in ductile cast iron. In Samuelson J, Marquis G, Solin J, editors. Competent Design by Castings—Improvements in a Nordic Project, Helsinki, Finland: VTT; 2005, pp. 63–86.

[24] Wang Z, Zhao W, Zhou Z, Juang S, Yu X, Wang Q. Effect of shrinkage porosity on mechanicalproperties of ferritic ductile iron. China Foundry 2013;10: 141–147.

[25] Čanžar P, Tonković Z, Kodvanj J. Microstructure influence on fatigue behaviour of nodular cast iron. Mater Sci Eng A. 2012;556: 88-99.

[26] Borsato T, Ferro P, Fabrizi A, Berto F, Carollo C. Long solidification time effect on solution strengthened ferritic ductile iron fatigue properties. Int J Fatigue 2021;145: 106137.

[27] Nadot Y, Mendez J, Ranganathan N, Beranger S. Fatigue life assessment of nodular cast iron containing casting defects. Fatigue Fract. Eng Mater Struct. 1999;22: 289-300.

[28] Nadot Y, Mendez J, Ranganathan N. Influence of casting defects on the fatigue limit of nodular cast iron. Int J Fatigue 2004;26: 311-319.

[29] Kainzinger P, Guster C, Severing M, Wolf A. Influence of micro-shrinkage on the fatigue behavior of ductile iron. In 13 International Conference on Fracture, Beijing, China, 2013.

[30] Nový F, Kopas P, Bokůvka O, Jambor M, Trško L. Influence of microscopic casting defects on fatigue endurance of ductile cast iron. MATEC Web Conf. 2018;157: 05019.

[31] Borsato T, Ferro P, Berto F, Carollo C. Mechanical and Fatigue Properties of Heavy Section Solution Strengthened Ferritic Ductile Iron Castings. Adv Eng Mater. 2016,18: 2070-2075.

[32] Borsato T, Ferro P, Berto F, Carollo C. Fatigue strength improvement of heavy-section pearlitic ductile iron castings by in-mould inoculation treatment. Int J Fatigue 2017;102: 221-227.

[33] Fernandino DO, Tenaglia N, Di Cocco V, Boeri RE, Iacoviello F. Relation between microstructural heterogeneities and damage mechanisms of a ferritic spheroidal graphite cast iron during tensile loading. Fatigue Fract Eng Mater Struct. 2020; 43: 1262– 1273

[34] Aghareb Parast MS, Jamalkhani Khameneh M, Azadi M, Azadi M, Mahdipanah MH, Roostaie S. Effect of plasma nitriding on high-cycle fatigue properties and fracture behaviors of GJS700 nodular cast iron under cyclic bending loading. Fatigue Fract Eng Mater Struct. 2021; 44: 2070– 2086.

[35] Murakami Y. Inclusion rating by statistics of extreme values and its application to fatigue strength prediction and quality control of materials. J Res Natl Inst Stand Technol. 1994;99:345.

[36] Murakami Y, Toriyama T, Coudert EM. Instructions for a new method of inclusion rating and correlations with the fatigue limit. J Test Eval. 1994;22: 318–326.

[37] Bauccio ML ASM Metals Reference Book. Materials Park, Ohio: ASM International; 1993

[38] Beretta S. Application of multiaxial fatigue criteria to materials containing defects. Fatigue Fract Eng Mater Struct. 2003;26: 551-559.

[39] Brownlee KA, Hodge JL, Rosenblatt M. The up- and down method with small samples. J Am Stat Assoc. 1953;48: 262-277.

[40] Machado PVS, Araújo LC, Venicius SM, Reis L, Araújo JA. Multiaxial fatigue assessment of steels with non-metallic inclusions by means of adapted critical plane criteria. Theor Appl Fract Mech. 2020;108: 102585.

NOMENCLATURE

$\hat{1},\hat{2},\hat{3}$	averaged directions of the principal stress axes
$\sqrt{area_n}_{max}$	square root of the expected maximum size of the defect under normal cyclic loading
$\sqrt{area_s}_{max}$	square root of the expected maximum size of the defect under shear cyclic loading
C_a	amplitude of the shear stress component on the critical plane
d	gauge section diameter
h_n	thickness associated to the inspection area under normal cyclic loading
HV	Vickers hardness
I	error index
L_0	gauge length
N_a	amplitude of the normal stress component perpendicular to the critical plane
$N_{eq,a}$	equivalent normal stress amplitude
N_{exp}	experimental number of loading cycles to failure
N_m	mean value of the normal stress component perpendicular to the critical plane
R	loading ratio
S_0	inspection area
$\mathbf{S_w}$	stress vector on the critical plane
T_n	return period related to normal cyclic loading
T_s	return period related to shear cyclic loading
T_{opt}	optimised return period
V	useful cross-section volume (prediction volume)
$V_{0,n}$	standard inspection volume related to normal cyclic loading
$V_{0,s}$	standard inspection volume related to shear cyclic loading

V_{max}	maximum value of the useful cross-section volume
$\mathbf{w}$	normal vector to the critical plane
β	phase shift between normal stress and shear stress
δ	off-angle defining the normal to the critical plane
θ_{cal}	theoretical orientation of the fracture plane
θ_{exp}	experimental orientation of the fracture plane
σ	applied normal stress
$\sigma_{af,-1}$	experimental material fatigue strength under fully reversed normal stress
$\sigma_{eq,a}$	equivalent stress amplitude
σ_u	material ultimate tensile strength
σ_w	fatigue limit under normal loading
τ	applied shear stress
$\tau_{af,-1}$	experimental material fatigue strength under fully reversed shear stress
τ_w	fatigue limit under torsion

Subscripts

a	amplitude
m	mean value

EFFECT OF THE POROSITY ON THE FATIGUE STRENGTH OF METALS

Sabrina Vantadori[a], Camilla Ronchei[b,*], Daniela Scorza[c],

Andrea Zanichelli[a], Raimondo Luciano[c]

[a] Department of Engineering & Architecture, University of Parma,
Parco Area delle Scienze 181/A, 43124 Parma, Italy
[b] Department of Civil Engineering, University of Calabria,
via Pietro Bucci, 87036 Arcavacata di Rende (CS), Italy
[c] Department of Engineering, University of Naples Parthenope,
Centro Direzionale Isola C4, 80143 Napoli, Italy

*Corresponding author: *camilla.ronchei@unical.it*

HIGHLIGHTS

1) A procedure for fatigue assessment of metals with solidification defects is employed
2) The fatigue behaviour of a DCI with a relevant micro-shrinkage porosity is analysed
3) A defect content analysis is performed by means of a statistical method deriving from EVT
4) The return period is computed by a relationship that optimises the procedure accuracy